

ASCA Temperature Maps of Three Clusters of Galaxies Abell 1060, AWM 7, and the Centaurus Cluster

T. FURUSHO,¹ N. Y. YAMASAKI,¹ T. OHASHI,¹ R. SHIBATA,² T. KAGEI,¹ Y. ISHISAKI,¹
K. KIKUCHI,³ H. EZAWA,⁴ and Y. IKEBE⁵

¹*Department of Physics, Tokyo Metropolitan University, 1-1 Minami-Ohsawa, Hachioji, Tokyo 192-0397*

E-mail(TF): furusho@phys.metro-u.ac.jp

²*Institute of Space and Astronautical Science, 3-1-1 Yoshinodai, Sagamihara, Kanagawa 229-8510*

³*Tsukuba Space Center, National Space Development Agency (NASDA), 2-1-1 Sengen, Ibaraki 305-8505*

⁴*Nobeyama Radio Observatory, National Astronomical Observatory, 462-2 Minamimaki, Minamisaku, Nagano 384-1305*

⁵*Max-Planck-Institute für extraterrestrische Physik, Postfach 1603, D-85740, Garching, Germany*

(Received ; accepted)

Abstract

We present two-dimensional temperature maps of three bright clusters of galaxies Abell 1060, AWM 7, and the Centaurus cluster, based on multi-pointing observations with the ASCA GIS. The temperatures are derived from hardness ratios by taking into account the XRT response. For the Centaurus cluster, we subtracted the central cool component using the previous ASCA and ROSAT results, and the metallicity gradients observed in AWM 7 and the Centaurus cluster were included in deriving the temperatures. The intracluster medium in Abell 1060 and AWM 7 is almost isothermal from the center to outer regions with a temperature of 3.3 and 3.9 keV, respectively. The Centaurus cluster exhibits remarkable hot regions within about 30' from the cluster center showing a temperature increase of +0.8 keV from the surrounding level of 3.5 keV, and outer cool regions with lower temperatures by -1.3 keV. These results imply that a strong merger has occurred in the Centaurus in the recent 2 – 3 Gyr, and the central cool component has survived it. In contrast, the gas in Abell 1060 was well-mixed in an early period, which probably has prevented the development of the central cool component. In AWM 7, mixing of the gas should have occurred in a period earlier than the epoch of metal enrichment.

Key words: galaxies: clusters: individual (Abell 1060, AWM 7, Centaurus Cluster) — galaxies: intergalactic medium — X-rays: galaxies

1. Introduction

Clusters of galaxies are filled with a diffuse, X-ray emitting hot plasma with temperatures typically a few $\times 10^7$ K. The primary energy source of the intracluster medium (ICM) is considered to be the kinetic energy released through the gas infall into the gravitational potential. The heating mechanism is, however, not yet fully understood. Numerical simulations predict that shock heatings are caused by mergers of smaller groups

and subclusters, and recent observations provide evidences as temperature structures. Mergers are considered to be the common phenomenon in the cluster evolution, which can be studied by the cluster morphologies and the temperature structures.

Another common feature in clusters of galaxies is the existence of a cool gas component in the cluster center. The presence and intensity of the cool components are recognized either from central narrow peaks in the surface brightness profiles or from X-ray spectra. The origin of the cool component has often been interpreted in terms of cooling flow models (e.g. Fabian 1994), in which dense gas in the cluster cores has radiative cooling times comparable to or shorter than the Hubble time. The cooling flow model requires a multi-phase temperature structure, whereas extensive cluster studies from ASCA spectroscopy have shown the co-existence of hot ($kT \gtrsim 3$ keV) and cool ($kT \sim 1$ keV) components in the central peaks. Strong connection between the cool component and the cD galaxy has been pointed out (Ikebe et al. 1999), and it is important to know when and how these cool components have been created in the course of cluster evolution.

Clusters with irregular morphologies and hot clusters with no central cool components often show significant temperature structures which are considered to be evidences of ongoing mergers (e.g. Markevitch et al. 1998). In particular, two-dimensional temperature maps of nearby clusters show detailed features with ASCA and various remarkable structures have been found. For example, hot regions larger than 100 kpc were discovered from the Coma (Honda et al. 1996; Donnelly et al. 1999; Watanabe et al. 1999) and the Virgo (Kikuchi et al. 2000; Shibata et al. 2001) clusters. In the Virgo cluster, the hot region with $kT \sim 4$ keV was twice higher than the surrounding regions. Under a merger scenario, the subcluster falls into the gravitational potential whose depth is characterized by the ICM temperature. If the infall occurs with the free-fall velocity which is about the same as the random velocity of the gas particles in the ICM, then the instantaneous rise of temperature after the collision is roughly by a factor of 2. This would be the maximum expected temperature, since the heat will quickly dissipate into the surrounding ICM.

To obtain a consistent view of the evolution of clusters with different sizes and morphologies, we need to look into temperature structures in symmetric clusters which show cool components. Numerical simulations show that temperature structures persist over several Gyr even after the surface brightness profile has been almost completely smoothed out (e.g. Schindler and Müller 1993). The Centaurus cluster, which has a strong central cool component (Fukazawa et al. 1994; Ikebe et al. 1999), shows a hot region at a few 100 kpc from the center (Churazov et al. 1999). Therefore, sensitive studies of the temperature distribution for a larger cluster sample and to their outer regions would bring us rich information.

This paper presents temperature maps of Abell 1060 (A1060 for short), AWM 7, and the Centaurus cluster (Abell 3526), based on the multi-pointing observations with ASCA (Tanaka et al. 1994). These clusters are all poor, nearby ($z = 0.0104 - 0.0172$), and bright clusters with the ICM temperatures $kT = 3 - 4$ keV. The closeness of these systems allows ASCA to resolve the temperature structures less than 100 kpc. The clusters are markedly different regarding the strength of the central cool component. The Centaurus cluster shows a very sharp central peak and strong cool component (Fukazawa et al. 1994; Allen and Fabian 1994; Ikebe et al. 1999). Strong metal concentration up to about 1.5 solar is seen, and a giant elliptical galaxy, NGC4696, exists as the cD galaxy. In contrast, A1060 does not show such a narrow peak and the X-ray surface brightness agrees well with a single β model from the center to a radius of $1h_{50}^{-1}$ Mpc. The metal abundance is flat with radius and the central cool component is very weak or absent (Tamura et al. 1996, 2000). These properties

No.]

are typical of non-cD clusters. Another cluster AWM 7 has a cD galaxy, NGC 1129, but the central X-ray peak is not as narrow nor intense as Centaurus. The metal concentration and the central cool emission are definitely weaker or more extended than the Centaurus (Neumann and Böhringer 1995; Xu et al. 1997; Ezawa et al. 1997). Therefore, AWM 7 falls in the middle of Centaurus and A1060 regarding the concentration of the cool component. For example, ratios of the cool-component luminosity to the total one are $\sim 10\%$, 6% , and $< 3\%$ for Centaurus, AWM 7, and A1060, respectively (Tamura et al. 1997). This difference may reflect the past history of the cluster evolution, such as a recent occurrence of mergers which might have disrupted a central cool component. Comparison of temperature maps among the three clusters is interesting in examining the connection between temperature structures and cD dominance.

Throughout this paper, we assume $H_0 = 50 \text{ km s}^{-1} \text{ Mpc}^{-1}$ and $q_0 = 0.5$. The solar number abundance of Fe relative to H is taken as 4.68×10^{-5} (Anders and Grevesse 1989).

2. Observations

2.1. ASCA observations and Data reduction

Table 1 shows the log of ASCA observations. The numbers of the pointings are 7, 6, and 11 for A1060, AWM 7, and Centaurus, respectively. Two pointings for A1060 have a very small separation angle ($\sim 2'$). We selected the GIS data with a cut-off rigidity $> 8 \text{ GV}$ and the telescope elevation angle $> 10^\circ$ and $> 5^\circ$ from the earth rim for day and night, respectively (see Ohashi et al. 1996 and Makishima et al. 1996 for the details of the GIS system). This paper deals with only the GIS results, since the field of view of the SIS ($11' \times 11'$) was unable to cover the whole cluster fields and not suitable for the present purpose.

Some of the spectra of A1060, taken in December 1999, showed significant excess emission in the energy range below 1 keV. The excess is thought to be due to scattered solar X-rays from the earth atmosphere, because a medium class solar flare occurred during the ASCA observation. By setting the elevation angle from the day earth to be $> 20^\circ$, this soft excess was eliminated. This condition was applied to all the A1060 data. The flare-like events due to the fluctuation of the particle background (Ishisaki 1996) were screened out, and the time periods after the attitude maneuver with unsettled pointing directions were excluded. The non X-ray and the cosmic X-ray backgrounds were estimated from the archival data taken during 1993–1994 (Ikebe 1995). Since all targets were observed during 1993–1999, we took into account the slow change in the intensity of the GIS non X-ray background (Ishisaki et al. 1997, ASCA News No. 5, 26). The long-term variation of the background count rate until 2000 indicated a factor of ~ 1.2 maximum around 1998 and an rms variation $\sim 7\%$.

The GIS2 images of the 3 clusters in the 0.7 – 7 keV band are shown in figures 1a–c. The circles show the GIS field of views with a radius of $22'$. The images were smoothed by a Gaussian function with $\sigma = 1'$ after subtraction of the non X-ray and the cosmic X-ray backgrounds and exposure correction. In the A1060 image in figure 1a, the source at $29'$ north-east of the cluster center is a group of galaxies, HCG 48 ($z = 0.0094$). Other clusters show no obvious substructures or intense point sources as bright as HCG 48.

2.2. ROSAT observations

For spatially extended sources, an analysis of the ASCA data needs proper consideration of the complicated response of the X-ray telescope (XRT; Serlemitsos et al. 1995) as described in the next section. To take these effects into account, we simulated the GIS observations using the two-dimensional ROSAT PSPC data in the

0.5 – 2.0 keV band as input images. The higher angular resolution than ASCA by several factors would allow such a substitution.

The ROSAT PSPC observed A1060 and AWM 7 on January 1 in 1992 and January 28 in 1992, respectively. The single pointings of the PSPC completely cover the GIS observed regions for these 2 clusters. For the Centaurus cluster, 5 PSPC pointings were conducted on February 2 in 1992 (the central pointing), July 25 in 1992 and January 16 – 25 in 1993 (the outer 4 pointings).

The data selection was carried out by looking into the time variation of the PSPC count rate in different pulse-height channels. Subtraction of non-cosmic background and correction for the vignetting were performed using the Extended Source Analysis Software package (Snowden et al. 1994). Assuming the axial symmetry, we fit the surface brightness profile in the energy range of 0.5 – 2.0 keV with a single β model (double β model for the Centaurus) added onto a constant level which corresponds to the cosmic X-ray background. The obtained β -model parameters are consistent with the previous results for A1060 by Tamura et al. (2000), AWM 7 by Neumann and Böhringer (1995), and Centaurus by Ikebe et al. (1999), respectively. Following this consistency check, we smoothed the two-dimensional PSPC images by a Gaussian function in order to suppress the statistical fluctuation. The gaussian width depended on the intensity: $\sigma = 60''$ and $15''$ for the intensity levels < 2 and $2 - 10$ cts pix^{-1} , respectively, and no smoothing for > 10 cts pix^{-1} . This procedure preserves the central sharpness of the images.

3. Analysis

3.1. Hardness ratio analysis

We estimated temperatures from hardness ratios (HR) rather than spectral fits, in order to maximize the spatial resolution of temperature maps. The energy division of the 2 energy bands was chosen so as to minimize the error of the resultant temperature for a temperature range of 3 – 4 keV. By evaluating $HR - kT$ relation for different energy divisions, we chose a common dividing energy of 2 keV for all 3 clusters. The definition of the hardness ratio is $HR = H/S$, where H and S are the count rates in 2 – 7 keV and 0.7 – 2 keV, respectively. The actual HR values are between 0.6 and 0.9 for all clusters.

The HR s and their statistical errors were calculated from the background subtracted data which were combined into a large image for each cluster from the ASCA multi-pointing observations. The HR s were converted to the temperature based on the $HR - kT$ relation. We assumed the incident spectra to be absorbed MEKAL models based on the previous ASCA results. The spectral parameters are shown in table 2. The same model was also used for the ray-tracing simulations. The parameters for A1060 were taken from Tamura et al. (2000). The N_{H} value is a little smaller than the Galactic value of 5×10^{20} cm^{-2} , and the metal abundance was fixed at $Z = 0.31$ solar. In AWM 7, the metallicity gradient was found by Ezawa et al. (1997). We included the effect in the $HR - kT$ relation and the ray-tracing simulation, assuming the abundance curve given in table 1 of Ezawa et al. (1997). The best-fit N_{H} value was consistent with the Galactic value. For the Centaurus cluster, the metallicity gradient observed by Ikebe et al. (1999; equation (5)) was used in our analysis. The effect of the abundance variation on temperature is less than ~ 0.13 keV in the Centaurus case. The best-fit N_{H} values obtained by Ikebe et al. (1999) differed with spectral models, but were consistent with the Galactic value (Stark et al. 1992). We therefore adopted the Galactic value here.

3.2. Correction on XRT Response

The XRT on-board ASCA has three main difficulties in performing spatially resolved spectral studies for sources which are extended more than the field of view: 1) energy-dependent decline of the effective area as a function of an off-axis angle from the optical axis (energy-dependent vignetting), 2) stray light from outside of the field of view (mainly from the bright cluster core in the present case), and 3) energy-dependence of the point spread function (PSF).

The first effect is dominant for observations of extended sources. The effective area of XRT at an off-axis angle of $20'$ from the optical axis decreases to $\sim 25\%$ and 10% for 2 and 8 keV, respectively. This difference, on the one hand, causes an underestimate of the HR value in the field edge, and complicates the data treatment, on the other hand, for overlapping regions of the multi-pointings even if the cluster is completely isothermal. Therefore, we ran ray-tracing simulations for isothermal clusters based on the PSPC image to correct for these effects.

Second, the stray light mixes the X-ray fluxes from different regions. This effect can be examined also with the ray-tracing simulation by tracing back the detected photons to their sky origins. Figure 2 shows fractions of the photon origins in 7 annuli with $r = 0' - 4' - 8' - 12' - 20' - 28' - 36' - 44'$. The fractions are calculated from the simulated image combined with all pointings for 3 clusters. The top curve shows the fraction coming from the pointed sky region, and the middle curve indicates contaminating fraction from brighter inner regions for each radius. The bottom curve is the contamination from outer regions. For the innermost region within a radius of $4'$, 80 – 90% of the detected photons come from the corresponding sky region. In the outer regions $r > 10'$, the fraction of this “direct” component reduces to 50 – 60% and remains to be about the same to a radius of $40'$. The contaminating flux mostly comes from inner regions, making the radial temperature distribution smoother than the true structure.

Regarding the last effect, the PSF always produces image distortions and has tails which depend on off-axis angles. In particular, the tail of the PSF is more extended in high energies than in lower energies. This energy-dependent effect is included in our simulation which reproduces the tail spectrum with 10% accuracy (Kunieda et al. 1995, ASCA News No. 3, 3). This effect becomes significant at an offset angle $r \sim 6'$, where the source flux drops to about $1/100$. Therefore, this PSF effect is not a significant problem in the present analysis.

Examples of the HR s are shown in figure 3, in which observed HR profiles in an azimuthal direction are compared with simulated values for a radius of $10' - 20'$ for three clusters. The error bars of the data are 90% statistical errors. For the simulated clusters, we assume an isothermal ICM with the average temperature for the hot component based on the previous ASCA studies as described before. The assumed spectral parameters are listed in table 2. Because of the XRT response, even the simulated HR s vary by about 5% from position to position. The HR s are in good agreement with the isothermal cluster in the case of A1060, while the Centaurus clearly shows significant deviations. We note that the isothermal models for the simulations also included the abundance gradients for AWM 7 and Centaurus as described in the previous subsection.

By taking the ratio of HR s between the data and the isothermal simulation for each cell of the image, the temperature maps were produced. The ratio in each cell gives a correction factor to the HR , and the corrected HR values and errors were then converted to the temperatures using an appropriate $HR - kT$ curve for the assumed metal abundance and N_{H} . Further details concerning the temperature estimation and systematic errors are described later in section 5.

3.3. Temperature maps

Based on the hardness ratio analysis, we produced two-dimensional temperature maps (see figure 4). The images were binned into a cell of $5' \times 5'$ for A1060 and AWM 7, and $2.5' \times 2.5'$ for Centaurus, since the Centaurus is much brighter than the others. These angular scales correspond to actual sizes of ~ 100 , 150 , and 50 kpc for A1060, AWM 7, and Centaurus, respectively. Furthermore, to suppress the fluctuation, we took an intensity-weighted average for 4×4 cells ($20' \times 20'$ for A1060 and AWM 7, $10' \times 10'$ for Centaurus). Therefore, the color-coded maps show running means of the temperature and sharp structures are suppressed. These running means were only adopted in the color representation in figure 4, and quantitative analysis was carried out on individual data. The temperature maps are shown for a spatial range where statistical errors in the 4×4 cells are less than 10% for A1060 and AWM 7, and less than 15% for Centaurus, respectively.

Since the color-coded maps give no information about the error, we present the temperature values for 7 annular regions in figure 5. The dividing radii are $r = 0' - 2' - 4' - 8' - 12' - 20' - 28' - 36'$, and the data points are mutually independent (no running means). Each ring at $r > 2'$ is equally divided to 8 azimuthal sections with an opening angle of 45° each, but 4 azimuthal sections with 90° for the $2' - 4'$ ring. The errors indicate 90% statistical errors.

To obtain detailed spectral information for selected regions, we also carried out spectral fits. Observed properties of individual clusters are described in detail below.

4. Results

4.1. A1060

The color-coded map in figure 4a shows that the temperature variation in A1060 is less than 15% of the average value in the whole cluster. The azimuthally averaged temperatures are shown in figure 5a. Fitting a model of constant value to the data in figure 5a gives the mean temperature of 3.26 ± 0.06 keV with $\chi^2/\nu = 57.2/44$. The error is the variance of mean at $\Delta\chi^2 = 2.706$ by the statistical errors only. The mean temperature is consistent with the previous results of 3.3 ± 0.1 keV from spectral fitting within the central $5'$ by Tamura et al. (1996, 2000).

Based on the temperature map, we accumulated the pulse-height spectra for selected regions. The south-east region (region #2 indicated in figure 6) suggests slightly higher temperature compared with the region #1, whose significance should be confirmed. We assumed an absorbed MEKAL model and the response for an isothermal cluster, which do not require a priori knowledge of the temperature distribution (as in Honda et al. 1996). The spectra and the best-fit models are shown in figure 6, and the ratios between data and the best-fit model for the medium-temperature region #1 (“med”) are shown in the bottom panel. The normalizations were arbitrarily scaled to help visual comparison. Results of the spectral fits are summarized in table 3. The 90% error ranges of the temperatures and metal abundances between #1 and #2 overlap with each other. Since no other regions suggest a larger deviation in temperature, we conclude that the ICM in A1060 is consistent to be isothermal.

4.2. AWM 7

Figure 4b shows the temperature map of AWM 7. The temperature variation in the whole cluster is again less than 15%. The central region within a radius of $20'$ is very isothermal, but there are some structures near the

No.]

north and south edges. In figure 5b, azimuthally averaged temperatures are shown with the mean temperature of 3.82 ± 0.06 keV from a constant-temperature fit with $\chi^2/\nu = 55.5/44$. The PSPC result indicates a temperature drop due to the cool component in the central $r < 2'$ region (Neumann and Böhringer 1995), however this cool component is very weak in the GIS data and the temperature after averaging over a $20' \times 20'$ region shows almost no signature. If this central region is excluded, the reduced chi-square becomes significantly smaller, $\chi^2/\nu = 42.1/43$ with the mean temperature of 3.85 ± 0.06 keV. Both of the mean temperatures agree with the cluster average of 3.9 ± 0.2 keV with the central pointing obtained by Markevitch and Vikhlinin (1997). They also derived a two-dimensional temperature map for the central pointing and found it isothermal.

The temperature map in figure 4b shows cool and hot features at $\sim 20'$ north and south of the cluster center. We also fit the spectra for these regions (regions #1 and #2 in figure 7) with absorbed MEKAL models, and the data, best-fit models, and ratios to the “cool” model are shown in figure 7. As shown in table 3, the best-fit temperatures are $3.6_{-0.4}^{+0.6}$ keV for the north and $4.6_{-0.7}^{+1.2}$ keV for the south regions. The temperature difference is larger than the 90% error but less than the 95% limit, so this feature has a marginal statistical significance.

4.3. Centaurus Cluster

Temperature map

Figure 4c shows the temperature map of the Centaurus cluster without any correction to the central cool component. The central region within $r < 30'$ shows a remarkable hot region $\sim 15'$ south east from the center, which was already reported by Churazov et al. (1999). However, since no corrections have been made for the central cool component, the inner envelope of the reported hot region may well be the outer boundary of the cool component. This point needs to be examined. Another interesting new feature is the extended cool regions at $40'$ north west and north east, indicating a temperature close to 2 keV. Figure 5c shows the azimuthally averaged temperatures. By fitting a constant model to the data of figure 5c, isothermal model was rejected at the 99.99% confidence with the mean temperature of 3.15 ± 0.03 keV (reduced chi-square of $\chi^2/\nu = 1110/44$).

Correction for the Cool Component

Since our main interest is the structure of the hot component, we have subtracted the cool component from the data assuming the model derived from Ikebe et al. (1999), who analyzed PSPC and GIS data jointly. The model gives radial profiles of the emission measure and filling factor with a cut off radius of $R_{\text{cut}} = 6'$ assuming a constant temperature, $kT_{\text{cool}} = 1.4$ keV, for the cool component. Using this model and the ray-tracing simulation, we can estimate the radial count-rate profiles for the hard and soft bands, which were simply subtracted from the data. The central intensity of the cool component was estimated here from the ratio of the emission integrals of the two components given in table 3 of Ikebe et al. (1999), which showed the best-fit parameters for the spectrum within the central $3'$ region fitted with a 2-temperature MEKAL model. Note that the number of photons subtracted as the cool component within the central $6'$ was about a quarter of the total.

Figure 4d shows the resultant temperature map for the hot component only. The difference between figure 4c and 4d mainly appears within the central $\sim 8'$ region as expected from the model profile of the cool component. The cluster center is fairly hot, and the obtained temperature (4.3 ± 0.4 keV) is close to the level in the south-east hot region. This temperature is consistent with the result ($4.2_{-0.3}^{+0.8}$ keV) by Ikebe et al. (1999). The azimuthally averaged temperatures are shown in figure 5d. The mean temperature for the data in figure 5d increases by 0.7

keV to 3.88 ± 0.05 keV. Again, the isothermal model was rejected with 99.99% confidence, though the reduced chi-square value became considerably smaller to $\chi^2/\nu = 125.8/44$.

Systematic errors in the subtraction process of the cool component need to be examined here. To avoid complications due to model parameters, we simply varied the cool-component intensity by $\pm 10\%$, by fixing its temperature and radial profile. This is an overestimation since the PSPC data can constrain the cool-component intensity with an accuracy of a few %. The 10% change causes a change of the hot-component temperature by 7% in the sense that stronger cool emission gives hotter temperature. Since the systematic error is comparable to the statistical error, we can say that the features in the temperature map has an accuracy of about 10%.

Spectra

To evaluate the significance of the hot and cool temperatures, pulse-height spectra for 3 selected regions were compared. The selected regions, their spectra, and the ratios of each data to the best-fit model for #1 are shown in figure 8, and results of spectral fits are shown in table 3. The region #2 in the south-east includes the hot region reported by Churazov et al. (1999), and the obtained temperature of 4.3 ± 0.2 keV is consistent with their result of 4.4 ± 0.2 keV. The region #1 is at nearly symmetric to the hot region with respect to the cluster center, which should reduce the systematic effects in the temperature comparison. The obtained temperature of 3.5 ± 0.1 keV is the typical value excluding the hot and cool regions. At 30' north-west, a cool region is seen in the temperature map (region #3). The spectral fit shows the temperature to be $2.2_{-0.3}^{+0.4}$ keV, which is significantly lower than the mean temperature.

5. Systematic errors

To confirm the significance of the temperature results, we need to look into systematic errors in the temperature determination process. There are 3 major origins to be considered: fluctuation of the cosmic (CXB) and non X-ray (NXB) backgrounds, error in the response function, and error in the assumed surface brightness profile.

5.1. Background uncertainty

The influence of the background fluctuation depends on the signal intensity, and outer regions of the cluster are considered to be more affected. Since both CXB and NXB have harder spectra than the observed clusters, their fluctuation can have a significant effect on the temperature results. We have studied this with a simulation by changing the background intensity. The fluctuation amplitude was chosen to be 10% for CXB and 7% for NXB, respectively, which are the typical values for the field to field variation, based on the previous studies (Ishisaki et al. 1997, ASCA News No. 5, 26).

Assuming the highest (+10% CXB and +7% NXB) and the lowest (−10% and −7%) background levels, we found that the temperatures at $r > 30'$ of A1060 changes by -0.2 and $+0.3$ keV on the average. The largest change in a single region ($5' \times 5'$) was -0.6 and $+0.8$ keV. Since other clusters have higher surface brightness than A1060 in the outer regions, we may take the systematic error of the temperature to be about 0.3 keV in the outermost regions and significantly smaller in the inner regions.

No.]

5.2. XRT response

Here we deal with the systematic errors due to the energy-dependence of the PSF and the effective area, and the stray light. The energy-dependent tail of the PSF comes the largest effect on the HR at $\sim 6'$ from the cluster center, where the tail is produced by the bright center. Figure 2 shows that the flux contamination at $r = 4' - 8'$ from the inner region is 25–35% of the detected flux. Combining this with the 10% systematic error in our simulation, the effect on the HR should be smaller than 3.5%, which corresponds to a temperature error of about 5%.

As for the error on the effective area, offset observations of the Crab nebula with the GIS showed the maximum fluctuation of photon index to be 2% for off-axis angles smaller than $22'$ (Fukazawa et al. 1997, ASCA News No. 5, 3). This corresponds to a HR error of 5.3% and results the temperature error of $\lesssim 8\%$. We have also performed several isothermal simulations for A1060 with temperatures between 2.7 keV and 3.6 keV. The $HR - kT$ relation at a large offset angle keeps an accuracy of 0.1 keV within a radius of $40'$.

The stray light of the XRT was studied by Ishisaki (1996) based on the Crab observations. The intensity of the stray light predicted by the ray-tracing simulation was shown to have an error of 15 – 20%. Figure 2 shows that fraction of the stray light, coming from offset angles $> 40'$, is at most 50% for all observed regions, causing an intensity error of about 10%. If all of this intensity falls in the hard band, we would observe 10% higher HR value than the true case. The spectrum of the stray light becomes harder for offset angles $\sim 30'$ and then softer for larger angles, but the spectral change is not very drastic. Considering this spectral behavior, we may assume that the systematic error of the HR is $\pm 5\%$ in the worst case. The change of HR value by 5%, causes the temperature change by about 10% for $kT = 3 - 4$ keV. Therefore, 10% of temperature is the conservative systematic error arising from our response estimation.

5.3. Surface brightness profile

Since the incident emission-measure profiles in calculating simulated clusters and response functions were based on the PSPC data, the difference in the sensitive energy ranges between PSPC and GIS might have caused some error in the present temperature results. The conversion factor from the PSPC count rate to emission measure varies by about 10% for a temperature range of 3–5 keV (Böhringer 1994). To investigate the systematic error due to the surface brightness profile, we first approximated the PSPC image with a β model and modified the model parameters. The two β models compared here are $\beta = 0.54$ and 0.61 , with a common core radius of $3.9'$. These parameters are given in table 2 of Tamura et al. (2000); the core radius and the lower β value are the best-fit values for the PSPC image, and the larger β is the maximum boundary value for the GIS fit, respectively. We took A1060 for this study because it has the lowest intensity. The variations of the temperature for the 2 models are 0.05 and 0.01 keV for $r < 30'$ and $r > 30'$, respectively, on the average. The largest difference in a single region ($5' \times 5'$) was 0.13 keV. Therefore, we may say that the error in the surface brightness model causes a fairly small systematic error.

5.4. Point sources

Possible influence from hard point sources to the temperature map was investigated. In figure 4c for the Centaurus cluster, a small hot region is seen at $35'$ south of the cluster center. The extent before taking the running mean is $\sim 2 \times 2$ cells ($5' \times 5'$), which is comparable to the point source image with the XRT response.

This peak is barely seen in the 0.7 – 7 keV band, however, the hard band image above 2 keV shows a clear peak. The position is identified as CCC 032 (Jerjen and Dressler 1997); a galaxy of morphological type Im at a redshift $z = 0.00913$. The temperature derived with an absorbed MEKAL model for the spectrum within a radius of $5'$ is about 7 keV, consistent with the indication of the temperature map. The absorbed X-ray flux in 0.5 – 10 keV is estimated to be 2.4×10^{-12} erg cm $^{-2}$ s $^{-1}$. However, about 70% of the flux is thought to be the cluster component according to the excess in the surface brightness. Therefore, the flux of about 7×10^{-13} erg cm $^{-2}$ s $^{-1}$ may be originated from the point source.

On the other hand, a compact group of galaxies HCG 48 at $29'$ off from the A1060 center shows no significant structure in the temperature map, figure 4a. In fact, a spectral fit gives a temperature of 3.3 keV, consistent with the A1060 ICM. We note that the X-ray emission peak does not correspond to the central elliptical galaxy in HCG 48, but to a Sa galaxy, ESO 501–G 059 at $2.6'$ south.

These results show that we can distinguish contaminations of point sources or galaxy groups with angular sizes $\sim 5'$ in terms of either distinct features in the temperature map or excess emission in the X-ray image. Since the extent of the hot region in Centaurus is considerably larger than the distinguishable size, it is unlikely that the temperature structures of the ICM are strongly affected by source contaminations.

6. Discussion

The present ASCA mapping observations have revealed significantly different temperature features in the nearby low-temperature ($kT \lesssim 4$ keV) clusters which show fairly symmetric ICM distribution. The difference is probably resulted from the past history of mergers. An interesting point is that there appear both hot and cool regions, as clearly recognized in the Centaurus cluster. Therefore, merging processes not only cause heating but probably bring in cool gas originally belonging to infalling subclusters to the ICM.

We have confirmed that the ICM of A1060 is almost isothermal with $kT \sim 3.3$ keV over the whole cluster region ($r \sim 1^\circ$). This suggests that A1060 has not experienced mergers during the recent a few Gyr. The metal abundance distribution is also uniform with a rather low value of 0.3 solar compared with the other 2 clusters. The constancy of metal abundance, as well as the constant temperature, suggests that the ICM in A1060 had been well mixed after an early starburst phase of $z \sim 1 - 2$ (Madau 1997) where metals have been injected into the ICM.

The cD galaxy of A1060, NGC 3311, is smaller than those in typical nearby bright clusters, and accordingly the central peak of the surface brightness accompanying the cool component is the weakest among the 3 clusters. The time scale of radiative cooling at the cluster center is calculated from the central density of 3×10^{-3} cm $^{-3}$ and the cooling function (Sutherland and Dopita 1993) to be about 4 Gyr, and the central cool gas would take ~ 10 Gyr or more to build up substantially. These features suggest that the formation process of A1060 has been rather slow. One reason could be that the number density of galaxies in the surrounding region is low. There is an empty space of about 60 – 70 Mpc extent in front and behind A1060 along the line of sight (Richter et al. 1982). The low matter density and the early mixing of the gas may have jointly acted to hold the growth speed of A1060.

As for AWM 7, the second system studied here, the central $r < 20'$ (~ 600 kpc) region shows an isothermal ICM with $kT \sim 3.9$ keV. There are small temperature deviations near the north and south edges of the cluster with a low significance of about 1.8σ (see table 3) between the hot and cool regions. The north region (#1)

shows a cooler temperature than the central region, and vice versa for the south region. Except for these north and south structures, the constant temperature suggests that mergers have not occurred for a few Gyr. In contrast to A1060, a large-scale metallicity gradient has been found in AWM 7 (Ezawa et al. 1997). A possible scenario based on these results is that the isothermality was already reached before the early starburst phase. If a gas mixing occurred recently, the metal distribution would become uniform and no more traces the galaxy distribution (see Metzler and Evrard 1994, Ezawa et al. 1997). This excludes the recent gas mixing in AWM 7, and the isothermality of the ICM also suggests no recent mergers for a few Gyr. The calculated cooling time from the central density of 0.01 cm^{-3} , $\sim 1 \text{ Gyr}$, is reasonably short and can explain that a significant amount of the cool gas has been accumulated during the prolonged non-merger period.

Another distinctive feature of AWM 7 is the elongated X-ray image in the east-west direction. This elongation is nearly parallel to the large-scale filament of the Pisces-Perseus supercluster. There is, however, no significant temperature structure along this direction as seen in figure 4b. Tidal deformation and directional mass accretion have been considered as possible origins of the elongated morphology (Neumann and Böhringer 1995). The tidal force from the Perseus cluster ($2 \times 10^{15} M_{\odot}$) was shown to deform the gas by only 2%, which is a factor of 5–10 too weak to cause the observed ellipticity. On the other hand, if the directional mass accretion takes the form of subcluster mergers, we would expect a clear temperature structure along the east-west direction. Since the tidal deformation itself would not cause large temperature variation, the constant temperature in AWM 7 suggests that the underlying dark matter may have an extended structure along the filament of the Pisces-Perseus supercluster.

The most remarkable result in the present observations is the temperature distribution of the Centaurus cluster. We have shown that the hot region reported by Churazov et al. (1999) is more extended and also covers the cluster center, which is seen after subtracting the cool component (figure 4d). Also, there are cool regions in the northeast and northwest near the cluster edge. The spectral fits show that the temperatures in the hot and cool regions differ by a factor of about 2, and the deviations from the surrounding values are $\pm 20 - 30\%$.

Since both the central and the southeast hot regions in the Centaurus show similar temperatures, $kT \sim 4.3 \text{ keV}$, they may have been heated in a single major merger. The radiative cooling time at the cluster center with an electron density of 0.02 cm^{-3} is about 0.5 Gyr, much less than the time for the temperature variation to be smoothed out. Therefore, the central cool component may have been accumulated recently, after the merger which have probably occurred a few Gyr ago. However, there is strong metal concentration in both the hot and the cool components (Fukazawa et al. 1994). The recent accumulation after the gas mixing due to the merger cannot explain this metallicity gradient, and the cool gas is more likely to have been built up at least before the last merger which has caused the temperature variation.

The stellar mass within the central 50 kpc of the Centaurus cluster is estimated to be $2 \times 10^{12} M_{\odot}$ (Ikebe et al. 1999). Such a mass concentration, i.e. the formation of the cD galaxy, must have started in a very early time. This suggests that the strong cool component has been established all the way through the early starburst phase until the beginning of the major merger. In this case, the central cool component was probably massive enough to survive the merger which have caused a shock heating and raised temperature by nearly 1 keV. Recently, Gómez et al. (2000) performed numerical simulations of head-on mergers in cooling-flow clusters. In cases where the initial cooling times are very small, even though the flows are once disrupted, the central cooling time remains less than the Hubble time and the flows are re-established in a few Gyr. These clusters would naturally

be classified as cooling-flow clusters even though they have experienced significant mergers. Regardless of the origin of the cool component, the Centaurus cluster may correspond to these cases of survived cool components.

7. Conclusion

Both A1060 and AWM 7 show isothermal ICM for the most part of the cluster region, and suggest that they have not experienced merging processes for recent a few Gyr. The difference in the metal abundance distribution imply that the gas mixing due to a merger occurred before and after the metal enrichment of the ICM in AWM 7 and A1060, respectively. Absence of a significant temperature structure along the elongation of the X-ray morphology of AWM 7 suggests a possibility that a tidal deformation by an unknown large gravitational potential may be working. The Centaurus cluster exhibits remarkable temperature structures characterized by the extended hot and outer cool regions. A shock heating due to a subcluster merger into the main gravitational potential can consistently explain the observed temperature increase by about 20–30%. It is likely that the central cool component was already established at the time of the merger, because the cool component shows strong metal concentration around the cD galaxy. Therefore, the central cool component in Centaurus was not disrupted by the major merger which has created the complicated temperature structure.

We appreciate the ASCA-ANL, SimASCA, and SimARF teams for the support of data analysis. We also thank Drs. S. Sasaki, M. Watanabe, and M. Takizawa for stimulating discussion and useful comments. This work was partly supported by the Grants-in Aid for Scientific Research No. 08404010 and No. 12304009 from the Japan Society for the Promotion of Science.

References

- Anders E., Grevesse N. 1989, *Geochim. Cosmochim. Acta* 53, 197
- Allen S.W., Fabian A.C. 1994, *MNRAS*, 269, 409
- Böhringer H. 1994, in *Cosmological Aspects of X-Ray Clusters of Galaxies*, ed W.C. Seitter (Kluwer Academic Publishers, Dordrecht, Boston, and London) v441, p123
- Churazov E., Gilfanov M., Forman W., Jones C. 1999, *ApJ*, 520, 105
- Donnelly R.H., Markevitch M., Forman W., Jones C., Churazov E., Gilfanov M. 1999, 513, 690
- Ezawa H., Fukazawa, Y., Makishima, K., Ohashi, T., Takahara, F., Xu, H., Yamasaki, N.Y. 1997, *ApJ*, 490, L33
- Fabian A.C. 1994, *ARA&A*, 32, 227
- Fukazawa, Y., Ohashi, T., Fabian, A. C., Canizares, C. R., Ikebe, Y., Makishima, K., Mushotzky, R. F., Yamashita, K. 1994, *PASJ*, 46, L55
- Gómez P. L., Loken C., Roettiger K., Burns J. O. 2000 *astro-ph/0009465*
- Honda H., Hirayama M., Watanabe M., Kunieda H., Tawara Y., Yamashita K., Ohashi T., Hughes J.P., Henry J.P. 1996, *ApJ* 473, L71
- Ikebe Y. 1995, PhD Thesis, The University of Tokyo
- Ikebe Y., Makishima K., Fukazawa Y., Tamura T., Xu H., Ohashi T., Matsushita K. 1999, *ApJ*, 525, 58
- Ishisaki, Y. 1996, PhD Thesis, The University of Tokyo
- Jerjen H., Dressler A. 1997, *A&AS*, 124, 1

- Kikuchi K., Itoh C., Kushino A., Furusho T., Matsushita K., Yamasaki N.Y., Ohashi T., Fukazawa, Y. et al. 2000, ApJL, 531, 95
- Madau P. 1997, in *Star Formation Near and Far*, ed S.S. Holt, L.G. Mundy (Woodbury, New York) 393, p481
- Makishima K., Tashiro M., Ebisawa K., Ezawa H., Fukazawa Y., Gunji S., Hirayama M., Idesawa E. et al. 1996, PASJ 48, 171
- Markevitch M., Vikhlinin A. 1997, ApJ, 474, 84
- Markevitch M., Forman W.R., Sarazin C.L., Vikhlinin A. 1998, ApJ, 503, 77
- Metzler C.A., Evrard A.E. 1994, ApJ, 437, 564
- Neumann D.M., Böhringer H. 1995, A&A, 301, 865
- Ohashi T., Ebisawa K. Fukazawa Y., Hiyoshi K., Horii M., Ikebe Y., Ikeda H., Inoue H. et al. 1996, PASJ 48, 157
- Richter O.-G., Materne J., Huchtmeier W.K. 1982, A&A, 111, 193
- Schindler S., Müller E. 1993, A&A, 272, 137
- Serlemitsos P.J., Jalota L., Soong Y., Kunieda H., Tawara Y., Tsusaka Y., Suzuki H., Sakima Y. et al. 1995, PASJ 47, 105
- Shibata R., Matsushita K., Yamasaki N.Y., Ohashi T., Ishida M., Kikuchi K., Böhringer H., Matsumoto H. 2001, ApJ, 549, in press (astro-ph/0010380)
- Snowden S.L., McCammon D., Burrows D.N., Mendenhall J.A. 1994, ApJ, 424, 714
- Stark A.A., Gammie C.F., Wilson R.W., Bally J., Linke R. 1992, ApJS, 79, 77
- Sutherland R.S., Dopita M.A. 1993, ApJS, 88, 253
- Tamura T., Day C.S., Fukazawa Y., Hatsukade I., Ikebe Y., Makishima K., Mushotzky R.F., Ohashi T. et al. 1996, PASJ, 48, 671
- Tamura T., Ikebe Y., Fukazawa Y., Makishima K., Ohashi T. 1997, in *X-ray Imaging and Spectroscopy of Cosmic Hot Plasmas*, ed F. Makino, K. Mitsuda (Universal Academy Press, Tokyo) p127
- Tamura T., Makishima K., Fukazawa Y., Ikebe Y., Xu H. 2000, ApJ, 535, 602
- Tanaka Y., Inoue H., Holt S.S. 1994, PASJ 46, L37
- Watanabe M., Yamashita K., Furuzawa A., Kunieda H., Tawara Y. 1999, ApJ, 527, 80
- Xu, H. et al. 1997, PASJ, 49, 9

Table 1. Log of ASCA observations

Cluster	Sequence No.	Date	Coordinates (J2000)		Exposure [†] (s)
			R.A.	Decl.	
A1060	80004000	93 Jun 28	159.42	-27.54	21940
	83024000	94 Dec 12	159.17	-27.08	6582
	83024010	94 Dec 19	159.17	-27.05	10451
	87009000	99 Dec 19	158.53	-27.23	14129
	87010000	99 Dec 20	159.27	-27.64	16385
	87011000	99 Dec 21	158.85	-27.96	10448
	87012000	99 Dec 21	158.39	-27.69	15502
AWM 7	80036000	93 Aug 7	43.46	41.42	9392
	80037000	93 Aug 7	43.06	41.40	14596
	81011000	94 Feb 10	44.27	41.78	7525
	81011010	94 Feb 10	43.32	41.78	13632
	81011020	94 Feb 11	43.88	42.20	12136
	81011030	94 Feb 11	43.88	41.62	10189
Centaurus	80032000	93 Jun 30	192.47	-41.23	11477
	80033000	93 Jul 5	192.55	-40.96	11326
	80034000	93 Jul 5	192.79	-41.32	8999
	83026000	95 Jul 19	192.46	-41.37	45899
	86000000	98 Feb 3	191.98	-40.58	6777
	86001000	98 Feb 3	191.28	-40.78	10580
	86002000	98 Feb 4	191.03	-41.30	7656
	86003000	98 Feb 4	191.31	-41.77	9634
	86004000	98 Feb 4	191.97	-41.87	8206
	86005000	98 Feb 5	192.50	-41.56	7706
	86006000	98 Feb 5	192.50	-41.01	11541

[†] The net exposure time after all the screening and cleaning procedures.

Table 2. Spectral model parameters and sequence numbers of PSPC observations of each cluster for the ray-tracing simulations.

Cluster	N_{H} (10^{20} cm^{-2})	kT (keV)	Z (solar)	PSPC observations Sequence no.
A1060	3.5	3.3	0.31	800200
AWM 7	8.7	3.6	0.51–0.16	800168
Centaurus	8.8	4.0	1.5–0.2	800192, 800321, 800322, 800323, 800324

Table 3. Results of the spectral fits for selected regions. The errors are statistical and 90%-confidence levels for single parameter of interest.

Cluster	region no. [†]	N_{H} (10^{20} cm^{-2})	kT (keV)	Z (solar)	$\chi^2/d.o.f$
A1060	#1 (med)	3.5(fix)	$3.00^{+0.14}_{-0.13}$	$0.44^{+0.14}_{-0.12}$	67.0/55
	#2 (hot)	3.5(fix)	$3.19^{+0.19}_{-0.18}$	$0.30^{+0.15}_{-0.13}$	60.1/55
AWM 7	#1 (cool)	8.7(fix)	$3.60^{+0.60}_{-0.44}$	$0.19^{+0.38}_{-0.19}$	22.5/18
	#2 (hot)	8.7(fix)	$4.61^{+1.16}_{-0.70}$	$0.35^{+0.58}_{-0.23}$	24.2/18
Centaurus	#1 (med)	8.8(fix)	$3.54^{+0.09}_{-0.09}$	$0.41^{+0.07}_{-0.07}$	47.8/45
	#2 (hot)	8.8(fix)	$4.31^{+0.17}_{-0.17}$	$0.32^{+0.09}_{-0.08}$	60.5/45
	#3 (cool)	8.8(fix)	$2.24^{+0.35}_{-0.30}$	$0.08^{+0.41}_{-0.08}$	11.1/14

[†] Corresponding regions are shown in figure 6–8.

Fig. 1. The GIS images of (a) A1060, (b) AWM 7, and (c) the Centaurus cluster in the energy range 0.7 – 7 keV. Circles with a radius of $22'$ show the GIS field of view. The images are smoothed by a Gaussian function with $\sigma = 1'$. The background is subtracted, and corrections for exposure time are performed.

Fig. 2. Fractions of the photon origin estimated from the ray-tracing simulation of the multi-pointing observations of the 3 clusters. The top curves indicate the flux coming from the observed region, and the curves in the middle and bottom show the contaminating fraction from inner and outer regions, respectively. The integrated radius of each annulus is shown as the thick bars only for A1060.

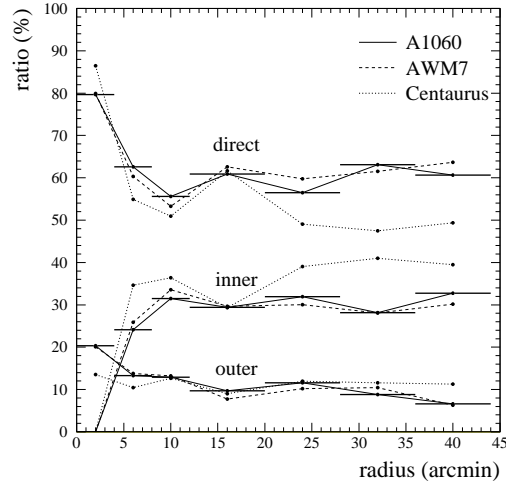


Fig. 3. Variation of the HR in the azimuthal direction with radius $10' - 20'$ for the three clusters. The filled circles show the observed values, and the solid lines show the simulated values for isothermal clusters. The error bars show 90% confidence levels.

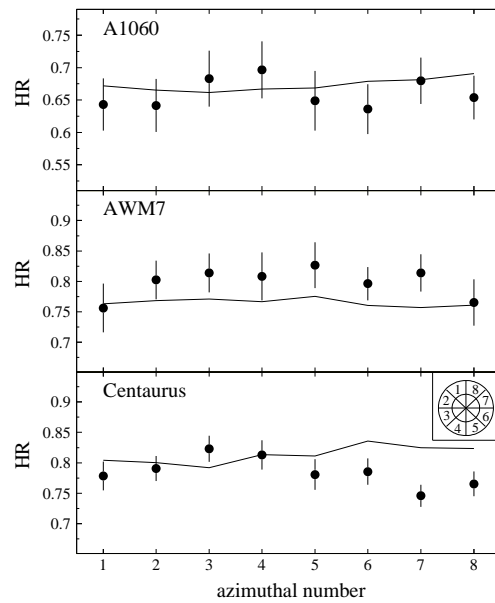


Fig. 4-a,b. Color-coded temperature maps for (a) A1060 and (b) AWM 7. The contours indicate X-ray intensity measured with the GIS.

Fig. 4-c,d. Color-coded temperature maps for the Centaurus cluster. The panel (c) shows results without correction for the central cool component. In the panel (d), the cool component was subtracted from the data based on the radial profile given by Ikebe et al. (1999).

Fig. 5-a,b. Azimuthal profiles of temperature in 7 annular regions for (a) A1060 and (b) AWM 7. The ring radii are indicated in the abscissa and each ring is divided to 8 azimuthal sections with an opening angle of 45° (4 sections with 90° for the innermost ring of $2' - 4'$) in a counterclockwise direction from the north. The error bars show 90% confidence levels. The solid lines show the mean temperatures by constant-temperature fits.

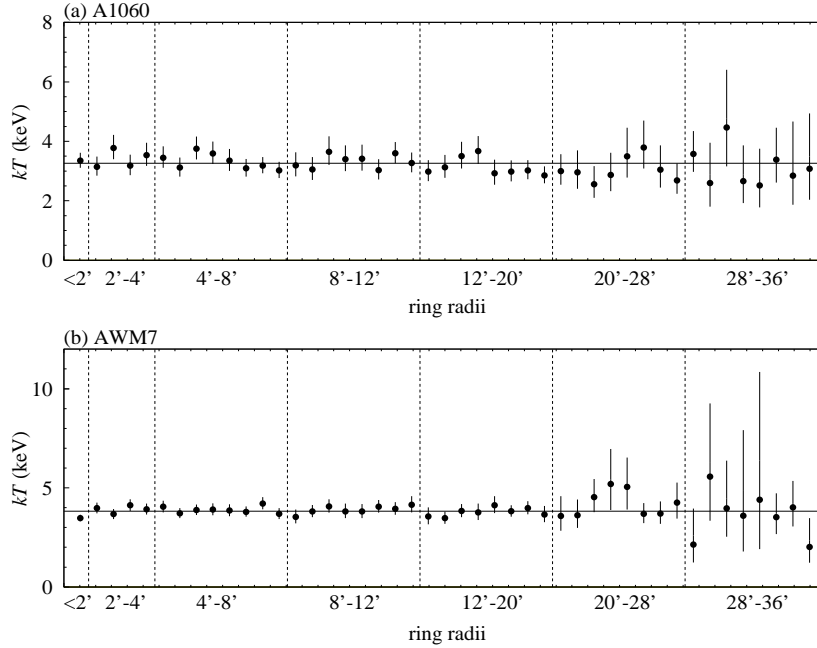


Fig. 5-c,d. Azimuthal temperature profiles for the Centaurus cluster, similar to the plots in figures 5(a) and (b). Figure 5 (c) and (d) are before and after the correction for the central cool component, respectively. The error bars in (d) are increased by including the systematic error of the cool-component intensity by 10%.

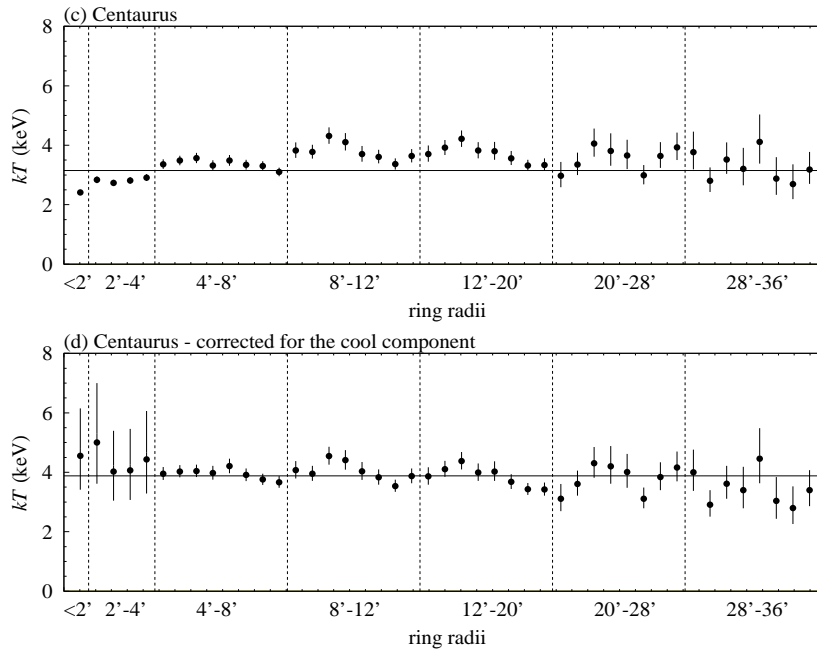


Fig. 6. Pulse-height spectra for two selected regions in A1060 fitted with thermal models. The bottom panels show data-to-model ratios for a common model, which is the best-fit model of #1 (“med”) shown by the thick line in the top panel. The right panel shows corresponding regions, in which the dashed circles show radii of $20'$ and $40'$.

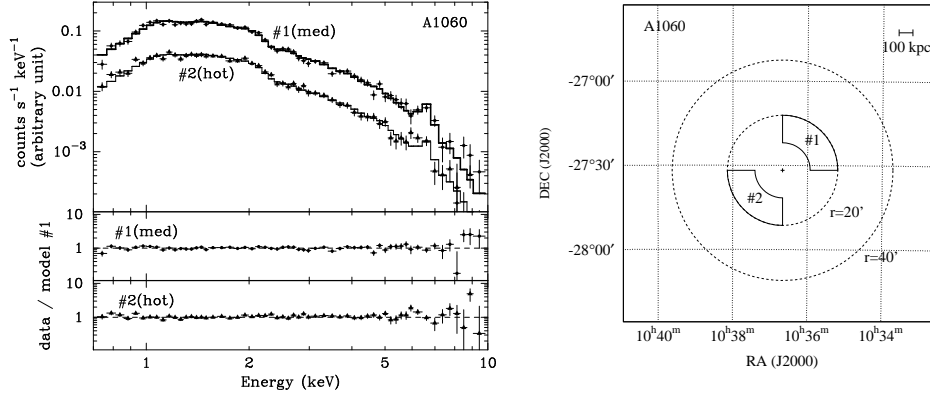


Fig. 7. Pulse-height spectra for two regions (top panel) in AWM 7, and normalized ratios to the best-fit model of #1 (bottom panel). The right panel shows the regions in the same way as in figure 6.

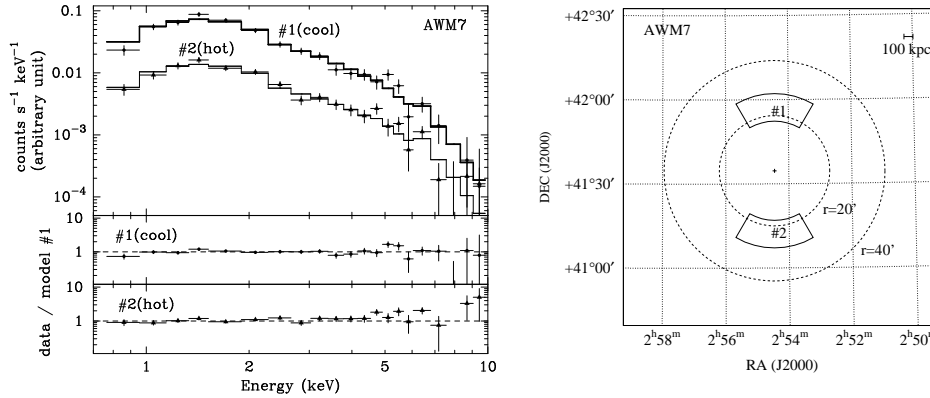
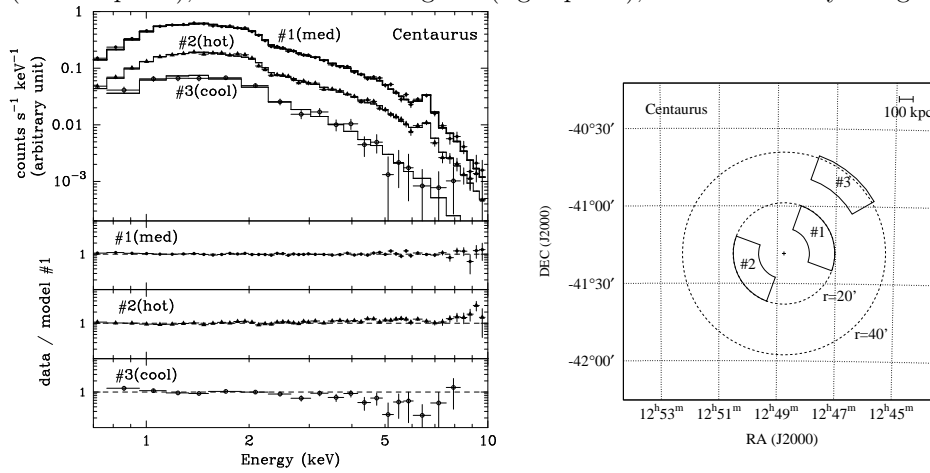


Fig. 8. Pulse-height spectra (top panel) for the Centaurus cluster, normalized ratios to the best-fit model of #1 (bottom panel), and the selected regions (right panel), in the same way as figure 6.



This figure "fig1a.jpg" is available in "jpg" format from:

<http://arxiv.org/ps/astro-ph/0103358v1>

This figure "fig1b.jpg" is available in "jpg" format from:

<http://arxiv.org/ps/astro-ph/0103358v1>

This figure "fig1c.jpg" is available in "jpg" format from:

<http://arxiv.org/ps/astro-ph/0103358v1>

This figure "fig4a.jpg" is available in "jpg" format from:

<http://arxiv.org/ps/astro-ph/0103358v1>

This figure "fig4b.jpg" is available in "jpg" format from:

<http://arxiv.org/ps/astro-ph/0103358v1>

This figure "fig4c.jpg" is available in "jpg" format from:

<http://arxiv.org/ps/astro-ph/0103358v1>

This figure "fig4d.jpg" is available in "jpg" format from:

<http://arxiv.org/ps/astro-ph/0103358v1>